Photoacoustics 4 (2016) 43–54

Contents lists available at ScienceDirect

Photoacoustics

journal homepage: www.elsevier.com/locate/pacs

# In vivo photoacoustic tomography of EGFR overexpressed in hepatocellular carcinoma mouse xenograft

Quan Zhou[a], Zhao Li[b], Juan Zhou[c], Bishnu P. Joshi[c], Gaoming Li[c], Xiyu Duan[a], Rork Kuick[d], Scott R. Owens[e], Thomas D. Wang[a,c,f,*]

[a] Department of Biomedical Engineering, University of Michigan, Ann Arbor, MI 48109, United States
[b] Department of Hepatobiliary Surgery, Peking University People's Hospital, Beijing, China
[c] Department of Medicine, Division of Gastroenterology, University of Michigan, Ann Arbor, MI 48109, United States
[d] Department of Biostatistics, University of Michigan, Ann Arbor, MI 48109, United States
[e] Department of Pathology, University of Michigan, Ann Arbor, MI 48109, United States
[f] Department of Mechanical Engineering, University of Michigan, Ann Arbor, MI 48109, United States

ARTICLE INFO

*Article history:*
Received 22 December 2015
Received in revised form 8 April 2016
Accepted 18 April 2016
Available online 22 April 2016

*Keywords:*
Hepatocellular carcinoma
Epidermal growth factor receptor (EGFR)
Photoacoustic
Imaging
Peptide

ABSTRACT

EGFR is a promising cell surface target for in vivo imaging that is highly overexpressed in hepatocellular carcinoma (HCC), a common cancer worldwide. Peptides penetrate easily into tumors for deep imaging, and clear rapidly from the circulation to minimize background. We aim to demonstrate use of an EGFR specific peptide to detect HCC xenograft tumors in mice with photoacoustic imaging. Nude mice implanted with human HCC cells that overexpress EGFR were injected intravenously with Cy5.5-labeled EGFR and scrambled control peptides respectively. Photoacoustic images collected from 0 to 24 h. Photoacoustic signal peaked in tumors at 3 h post-injection. Images from 0 to 1.8 cm beneath the skin revealed increased target-to-background (T/B) ratio from tumors. The T/B ratio was significantly greater for the EGFR versus control peptide. Clearance of signal was observed by ~24 h. EGFR overexpression was validated with immunofluorescence and immunohistochemistry. A peptide specific for EGFR delivered systemically can detect HCC xenograft tumors in vivo with photoacoustic imaging.


## 1. Introduction

Worldwide, hepatocellular carcinoma (HCC) is one of the most lethal cancers, causing ~745,000 deaths annually [1]. The prognosis for HCC is poor with a 5-year survival rate of <5%. Surgical resection remains the primary therapy [2,3]. However, the incidence of tumor recurrence is >50% [4]. Symptoms of HCC typically do not appear until a late stage. Only 10–20% of HCC tumors are diagnosed early enough for effective surgery [5–7]. Poor prognosis is due in part to a lack of effective and accurate early diagnostic methods, limiting treatment options. Patients with cirrhosis are at increased risk for developing HCC, and represent an important surveillance population [8–10]. New imaging techniques may improve the sensitivity and accuracy for early detection of HCC. Photoacoustic imaging is an emerging imaging modality that uses the combination of light for absorption and sound for emission. Compared with ultrasound, it offers higher resolution and capability for targeted detection.

Targeted imaging may improve specificity for detection of HCC. The epidermal growth factor receptor (EGFR) pathway plays an essential role in cell proliferation, survival and migration and its altered activity has been implicated in the development and growth of many tumors including HCC [11–13]. In previous studies, EGFR has been found to be overexpressed in 40–70% of HCC [14–19], most likely contributing to aggressive growth characteristics [20,21], metastasis formation, and resistance to therapy [17,22–24]. The EGFR inhibitor Gefitinib has been found to significantly reduce the incidence of HCC in an animal model [15]. EGFR is also overexpressed by other cancers, including lung [25], breast [26], pancreas [27], head and neck [28], and esophagus [29]. EGFR represents an attractive target for biologics (such as peptide and affibody [30] or antibodies in applications such as tumor-targeted imaging and therapy.

We have previously developed a peptide specific for EGFR [31]. Peptides have small size and low molecular weight that result in

*Abbreviations:* AU, arbitrary units; EGFR, epidermal growth factor receptor; HCC, hepatocellular carcinoma; PA, photoacoustic; T/B, target-to-background.

* Corresponding author at: Department of Medicine, Division of Gastroenterology, University of Michigan, 109 Zina Pitcher Pl. BSRB 1522, Ann Arbor, MI 48109-2200, United States.
*E-mail address:* thomaswa@umich.edu (T.D. Wang).

http://dx.doi.org/10.1016/j.pacs.2016.04.001

ideal pharmacokinetic properties for deep tissue imaging. Compared with bulky monoclonal antibodies, peptides provide an attractive alternative for visualizing tissue targets that would otherwise be difficult to penetrate or access [32]. Peptides clear rapidly from non-target tissues, resulting in reduced background. Peptides can be structurally altered to improve stability against proteolytic degradation, increase circulatory half-life, and enhance capillary permeability [33]. All of these attributes promote deep penetration into tissue and more effective targeting. Here, we aim to demonstrate the use of a peptide specific for EGFR to target HCC tumors in a pre-clinical xenograft model.

## 2. Methodology

### 2.1. Synthesis of photoacoustic imaging agents

Monomeric linear peptides QRHKPRE, hereafter QRH*, and its scrambled control PEHKRRQ, hereafter PEH*, (molecular weight = 1334.73 for both peptides) were synthesized with linker GGGSK using standard Fmoc-mediated solid-phase synthesis [31]. The C-terminal lysine was incorporated as Fmoc-Lys (ivDde)- OH, and the N-terminal amino acid was incorporated with Boc protection to avoid unwanted Fmoc removal during deprotection of the ivDde moiety prior to labeling. The ivDde side chain protecting group was removed with 5% hydrazine in DMF ($3 \times 10$ min) with continuous shaking at room temperature (RT). QRH*-Cy5.5 and PEH*-Cy5.5 were synthesized by coupling QRH* and PEH* with water soluble sulfo-Cy5.5- N-hydroxysuccinimide ester (Lumiprobe LLC) respectively overnight with N,N-diisopropylethylamine, followed by HPLC purification. The final purity was confirmed by analytical C18-column. Further characterization was performed with exact mass measurement by Q-TOF (Agilent Technologies) mass spec with ESI (Waters Inc) detection. After lyophilization, the peptides were stored at −80 °C and dissolved in water at a concentration of 300 μM before injection. The absorption spectrum was measured at 100 μM concentration with a UV–vis spectrophotometer in the 500–900 nm range (NanoDrop 2000, Thermo Scientific). Molecular graphics and analyses of the peptides were performed with the UCSF Chimera package (v. 1.10.2, University of California, San Francisco).

### 2.2. HCC xenograft tumor

Human HCC cells SK-Hep1, HepG2, and Hep3B were purchased from the ATCC (Manassas, VA) and cultured in Eagle's Minimum Essential Medium (EMEM). All cells were cultured at 37 °C in 5% $CO_2$, and supplemented with 10% fetal bovine serum (FBS) and 1% penicillin/streptomycin. Western blot was performed using a 1:1000 dilution of primary polyclonal rabbit anti-EGFR antibody (#2232S, Cell Signaling Technology) per manufacturer instructions. Loading was controlled with a 1:500 dilution of monoclonal mouse anti-β-tubulin (#32-2600, Invitrogen). SK-Hep1 cells were diluted in growth factor reduced (GFR) Matrigel Matrix (Corning), and injected into one flank of female (to avoid male dominance within a cage) nude athymic mice (nu/nu, Jackson Laboratory) at 4–6 weeks of age with weight between 20 and 25 g. $\sim 5 \times 10^6$ cells were implanted per mouse. Anesthesia was induced and maintained via a nose cone with inhaled isoflurane mixed with oxygen at a concentration of 2–4% at a flow rate of ~0.5 L/min for all in vivo animal experiments.

### 2.3. Confocal fluorescence microscopy

$\sim 10^3$ cells were grown on coverslips to ~80% confluence, washed once with PBS, and incubated with 5 μM QRH*-Cy5.5 and PEH*-Cy5.5 for 10 min at RT. The cells were then washed 3X in PBS, fixed with 4% PFA for 5 min, washed with PBS, and then mounted on glass slides with ProLong Gold reagent containing DAPI (Invitrogen). Confocal microscopy (Leica Inverted SP5X) was performed using a 63X oil-immersion objective. Fluorescence intensities from 5 cells in 2 independent images were quantified using custom Matlab (Mathworks) software.

### 2.4. Ultrasound imaging

2D ultrasound (US) images were collected from each xenograft tumor using a portable ultrasound scanner (SonixTablet, Ultrasonix, Analogic Corp.) designed for small animal imaging. During image acquisition, the mice were placed on a heated stage. Anesthesia was induced and maintained with 2% isofluorane (Fluriso; MWI Veterinary Supply Co.). Warmed (37 °C) ultrasound gel (Aquasonic 100, Parker Laboratories) was applied to the tumors. The ultrasound transducer (40 MHz) was used in B-mode, and translated along the length and width of the tumor. 3 images were taken in each direction to calculate tumor volume. Each image had a $12 \times 12$ mm$^2$ field of view with an in-plane pixel resolution of $50 \times 50$ μm$^2$ [34].

Ellipsoid volumes were estimated using πabc/6, where a, b, and c are dimensions measured from the US images. a is defined by the largest dimension in the sagittal plane, while b is the value perpendicular to a. c is the parameter orthogonal to both a and b in the transverse plane. Each measurement was performed 3 times [35].

### 2.5. MRI imaging

Tumor size was confirmed with MRI images collected with a 7T horizontal bore small animal MRI system (SGRAD 205/120/HD/S, Agilent Technologies) using a volume-based transmit/receive quadrature radio frequency coil with an inner diameter of 3.5 cm. The animals were given an intra-peritoneal (i.p.) injection of macrocyclic gadolinium chelate (Gadoteridol, ProHance) at a dose of 2.5 mmol Gd/kg body weight. Body temperature was maintained at 37 °C by blowing hot air into the magnet through a feedback control system. ~12–15 min after injection of gadolinium, transverse T1-weighted sections were acquired with a scout sequence in 3 orthogonal axes to identify tumor location. A $256 \times 128$ matrix was obtained in 5 min by conventional spin-echo multi-slice pulse sequence using repetition time (TR) = 8.5 ms, echo time (TE) = 2.6 ms, average = 2, in-plane field of view (FOV) = $35 \times 35$ mm$^2$, 25-mm slab thickness of 1 mm thick interleaved slices with no gap in between. Tumor volume was assessed with the freehand region of interest (ROI) function of NIH Image J software. Areas were measured on each MRI slice (1 mm thickness) and added together to reconstruct the 3D tumor volume.

### 2.6. Photoacoustic images of HCC xenograft tumor in vivo

We used a photoacoustic tomography system (Nexus128, Endra Inc.) that provides laser excitation at 7 ns pulses, 20 Hz repetition rate, 25 mJ/pulse, and wavelength range 680–950 nm. Ultrasound is collected by 128 unfocused 3 mm diameter transducers with 5 MHz center frequency arranged in a helical pattern in a hemispherical bowl filled with water, Fig. 1A. A transparent imaging tray located above the transducers was used to contain anesthetized animals. The console also includes data acquisition/reconstruction software, servo motors to rotate the bowl, and a temperature monitor. We optimized the imaging protocol to collect 120 views with 10 pulses/view, covering an imaging volume of $25 \times 25 \times 25$ mm$^3$ with a voxel size of 280 μm$^3$. Each dataset required ~2 min for acquisition. The animals were administered QRH*-Cy5.5 at 300 μM in 250 μL (75 nmol), and placed inside the

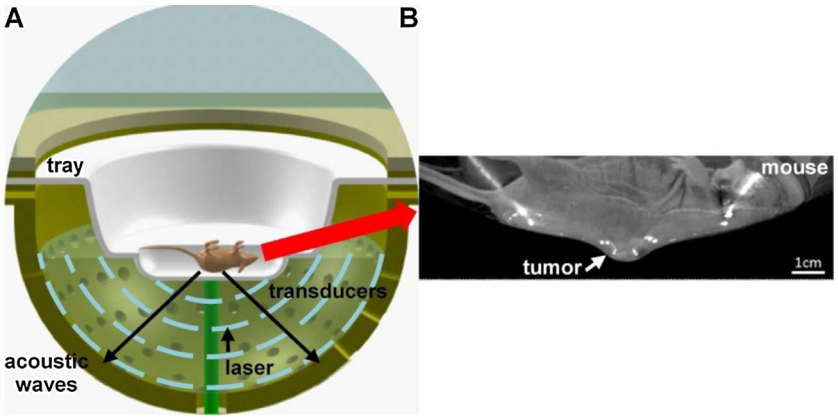


**Fig. 1.** Schematic of imaging system. (A) Laser pulses at λ = 680 nm (green) are absorbed by the tumor to produce acoustic waves that are detected by 128 ultrasound transducers arranged in a helical pattern. Water between the imaging tray and transducer array provides acoustic coupling. (B) Photograph of live animal under anesthesia with tumor positioned inside a dimple in the center of the tray. (For interpretation of the references to colour in this figure legend, the reader is referred to the web version of this article.)

tray with the subcutaneous tumor positioned inside a water-filled dimple to couple the ultrasound signal, Fig. 1B. We acquired images with $\lambda_{ex}$ = 680 nm at 0, 1, 3, 6, 12, and 24 h. A preliminary study was performed to determine wash out time after injecting either peptide (target or control), and whether the order of injection affected the photoacoustic signal level.

The 3D image was reconstructed after completion of imaging using data acquired from all 128 transducers at each view with a back-projection algorithm [36]. This algorithm corrects for pulse to pulse variations in laser intensity and small changes in temperature that affect the velocity of acoustic waves in water. The reconstructed raw data was analyzed using Osirix 6.5.2 software (Pixmeo) to generate a maximum intensity projection (MIP) image, which was converted to a color map using Matlab (R2013a, ver 8.1, Mathworks) software. Imaging was repeated with PEH*-Cy5.5 and Cy5.5 alone (dye without peptide) 48 h later in the same animals after the target peptide had cleared. 3D visualization of the reconstructed photoacoustic signals was performed using Amira

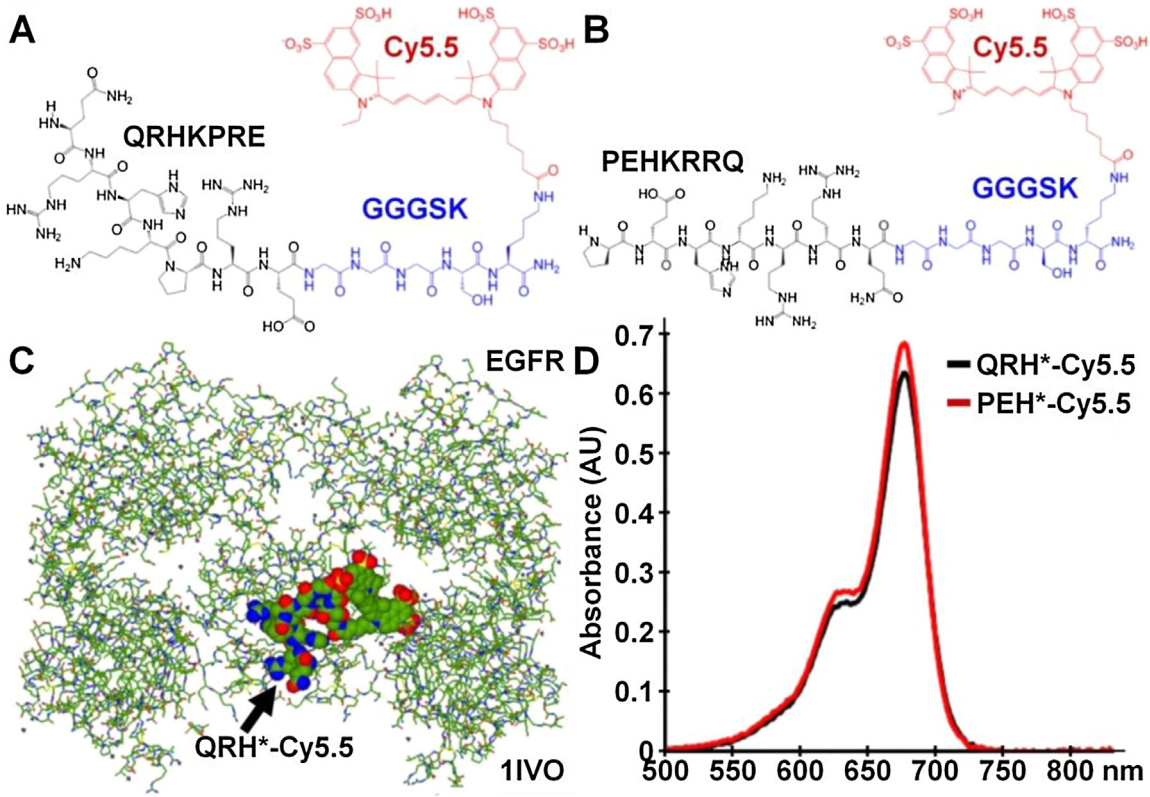


**Fig. 2.** Photoacoustic contrast agent specific for EGFR. (A) Chemical structure of QRHKPRE peptide (black) with GGGSK linker (blue) and Cy5.5 fluorophore (red), hereafter QRH*-Cy5.5. (B) Scrambled control peptide PEHKRRQ, hereafter PEH*-Cy5.5. (C) QRH*-Cy5.5 was found on the structural model (1IVO) to bind EGFR domain 2. (D) Absorbance spectra of Cy5.5-labeled peptides shows peak at $\lambda_{ex}$ = 677 nm. (For interpretation of the references to colour in this figure legend, the reader is referred to the web version of this article.)

software (ver 5.4.3, FEI Corporation), including volume rendering technique (VRT) with specular shading and color map for physics. The alpha value was set at 0.7 in order to reveal blood vessel structures underneath the tissue surface.

### 2.7. Validation of EGFR binding ex vivo with immunohistochemistry

Resected tumor and normal liver were fixed in 10% buffered formalin and paraffin embedded. 10 μm thick serial sections were cut and deparaffinized. Briefly, sections were incubated in xylene 3X for 3 min, washed with 100% ethanol 2X for 2 min, and washed with 95% ethanol 2X for 2 min. Rehydration was performed by washing the sections twice in $dH_2O$ for 5 min. Antigen unmasking was performed using Protease XXV (#AP-9006-002, Thermo Scientific) at 1 mg/mL in PBS buffer with pH 7.4 and digested for 15 min at 37 °C. The sections were washed 3X in $dH_2O$ for 3 min, and then incubated in 3% $H_2O_2$ in $H_2O$ for 10 min. The sections were washed 3X in $dH_2O$ for 2 min and in PBST for 5 min. Blocking was performed with DAKO protein blocking agent (X0909, DAKO) for 1 h at RT. We used 1:250 dilution of monoclonal mouse anti-EGFR antibody (clone 111.6, Thermo Scientific). The sections were incubated overnight in primary antibody at 4 °C and then washed in PBS 3X for 5 min. A 1:200 dilution of secondary antibody (goat anti-mouse) was added to each section and incubated for 30 min at RT. The secondary antibody solution was removed by washing 3X with PBS for 5 min. Premixed Elite Vectastain ABC reagent (Vector Labs) was added to each section and incubated for 30 min at RT. The sections were washed 3X in PBST for 5 min, and developed with 3,3′-diaminobenzidine substrate. The reaction was monitored for 1 min, and then quenched by immersing the slides in $dH_2O$. Hematoxylin was added as a counterstain for ~20 s, and the sections were dehydrated in increasing concentrations of ethyl alcohol (70%, 80%, 2X at 95%, 2X at 100%). Coverslips were attached using permount mounting medium (#SP15-100, Fisher) in xylene. Serial sections were processed for histology (H&E). Controls were prepared using secondary antibody, Elite Vectastain ABC reagent, Vector Labs and 3,3′-diaminobenzidine (without primary anti-EGFR antibody).

### 2.8. Validation of EGFR binding ex vivo with immunofluorescence

Resected tumor and normal liver (n = 24 mice) were formalin-fixed, paraffin embedded and cut in 10 μm thick sections. Deparaffinization, rehydration and antigen unmasking was performed, as described previously. Blocking was performed with DAKO protein blocking agent (X0909, DAKO) for 1 h at RT.

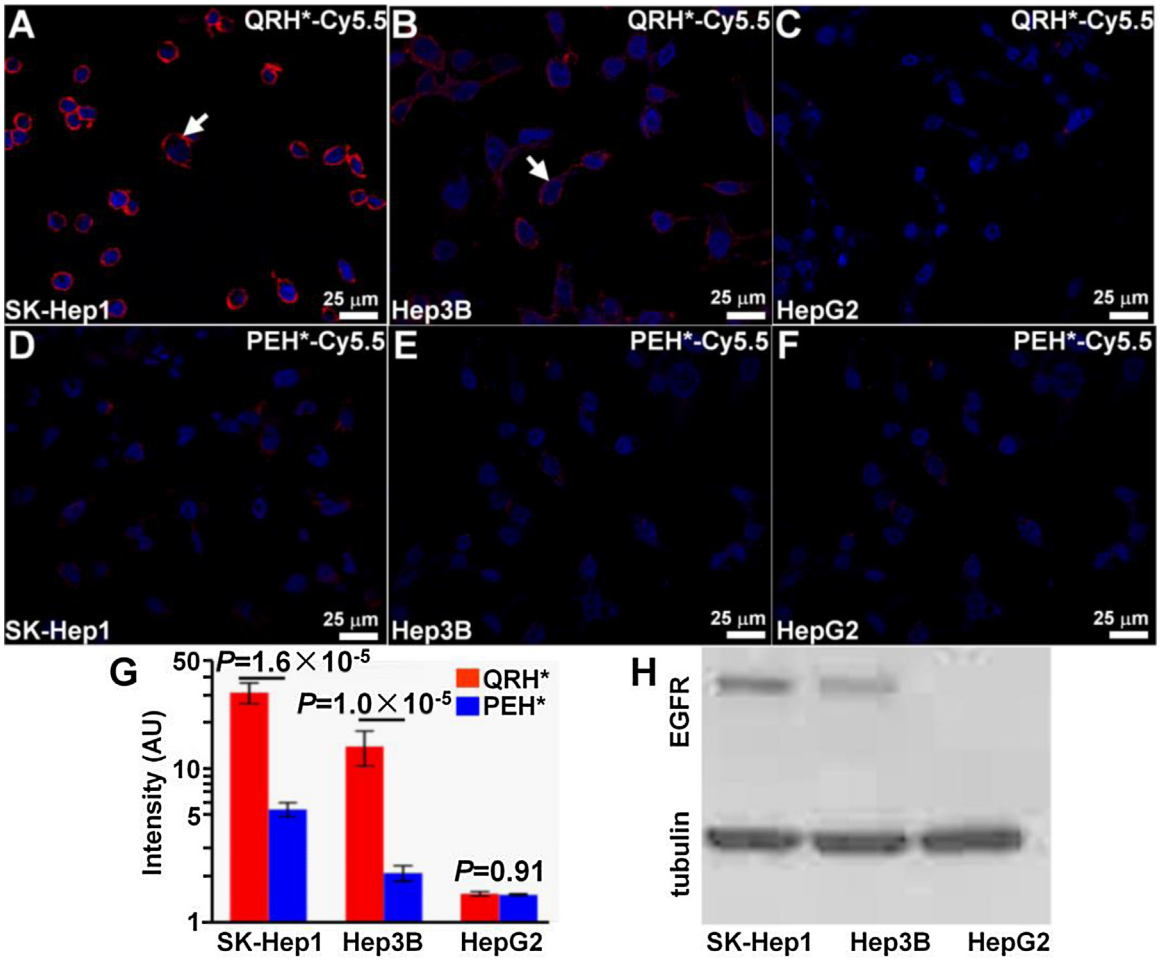


**Fig. 3.** Specific peptide binding to EGFR overexpressed in HCC cells. On confocal microscopy, we observed fluorescence at the surface (arrow) of (A) SK-Hep1, (B) Hep3B, and (C) HepG2 cells that have different levels of EGFR expression after incubation with QRH*-Cy5.5. (D–F) Minimal signal is observed with PEH*-Cy5.5 for all cells. (G) Quantified measurements show that QRH*-Cy5.5 has significantly greater intensities than PEH*-Cy5.5 on binding to SK-Hep1 and Hep3B cells (5.72 and 6.57 fold-change, $P = 1.63 \times 10^{-5}$ and $1.05 \times 10^{-5}$, respectively). A non-significant difference was found for HepG2 cells (1.02 fold-change, $P = 0.91$). Differences between QRH*-Cy5.5 and PEH*-Cy5.5 for SK-Hep1 and Hep3B were significantly greater than that for HepG2 (5.63 and 6.46 fold-change, $P = 1.25 \times 10^{-4}$ and $8.12 \times 10^{-5}$, respectively). We fitted two-way ANOVA models with terms for 3 cell lines, 2 peptides, and their interactions to log-transformed data. Measurements are an average of 5 randomly chosen cells on 2 slides for each condition. (H) Western blot shows EGFR expression levels for HCC cells.

Sections were then incubated with 5 μM QRH*-Cy5.5 in 2% BSA for 10 min at RT. The sections were washed 3X with PBS and mounted with Prolong Gold reagent containing DAPI (Invitrogen). Confocal microscopy was performed using $\lambda_{ex}$ = 670 and 405 nm for Cy5.5 and DAPI, respectively, at 63X magnification. Fluorescence intensities were measured from 3 randomly positioned boxes with dimensions of $20 \times 20\ \mu m^2$. Regions that showed intensity saturation were avoided.

### 2.9. Image analysis

The mean photoacoustic intensity in the target region was measured using the circular ROI function on 2D MIP photoacoustic images in Osirix 6.5.2 software with tumor dimensions measured using US (diameter of circle provided by arithmetic mean of dimensions a and c). The mean background was measured from the adjacent annulus with equal area. The target-to-background (T/B) ratio was calculated. Prism software (v6.02, GraphPad) was used to plot all data.

## 3. Results

### 3.1. Photoacoustic contrast agent specific for EGFR

QRHKPRE (black) was labeled on the C-terminus with Cy5.5 (red) via a GGGSK linker (blue), Fig. 2A. Using a structural model, we found a binding energy of $E_t$ = −554.81 kcal/mol for docking to EGFR (1IVO) [31]. By comparison, we found $E_t$ = −535.37 kcal/mol for the scrambled (control) peptide, PEH*-Cy5.5, Fig. 2B. In the model, QRH*-Cy5.5 binds to amino acids 230–310 of EGFR (domain 2), Fig. 2C. The absorption spectra of QRH*-Cy5.5 and PEH*-Cy5.5 at 100 μM concentration in water shows a peak at $\lambda_{abs}$ = 677 nm, Fig. 2D. We purified the Cy5.5-labeled peptides to >95% on HPLC. This result was confirmed on mass spectrometry. We found a molecular weight of 2232.88 g/mol, which agrees with the expected value, Fig. S1A,B. 3D surface structures of labeled targeting and scrambled control peptides are shown in Fig. S2A,B.

### 3.2. Specific binding to EGFR overexpressed in HCC cells

On confocal microscopy, we assessed binding of QRH*-Cy5.5 and PEH*-Cy5.5 to human HCC cells SK-Hep1, Hep3B, and HepG2 cells that express different levels of EGFR, respectively. For QRH*-Cy5.5, we observed different strengths of binding to the cell surface (arrows), Fig. 3A–C. Minimal binding was observed for PEH*-Cy5.5 (control) to all cells, Fig. 3D–F. We measured significantly greater fluorescence intensity from QRH*-Cy5.5 compared to PEH*-Cy5.5 for SK-Hep1 and Hep3B cells but not for HepG2, Fig. 3G. Also, the QRH*-Cy5.5 versus PEH*-Cy5.5 differences were significantly larger for SK-Hep1 and Hep3B than for HepG2. Western blot of cells is shown, Fig. 3H.

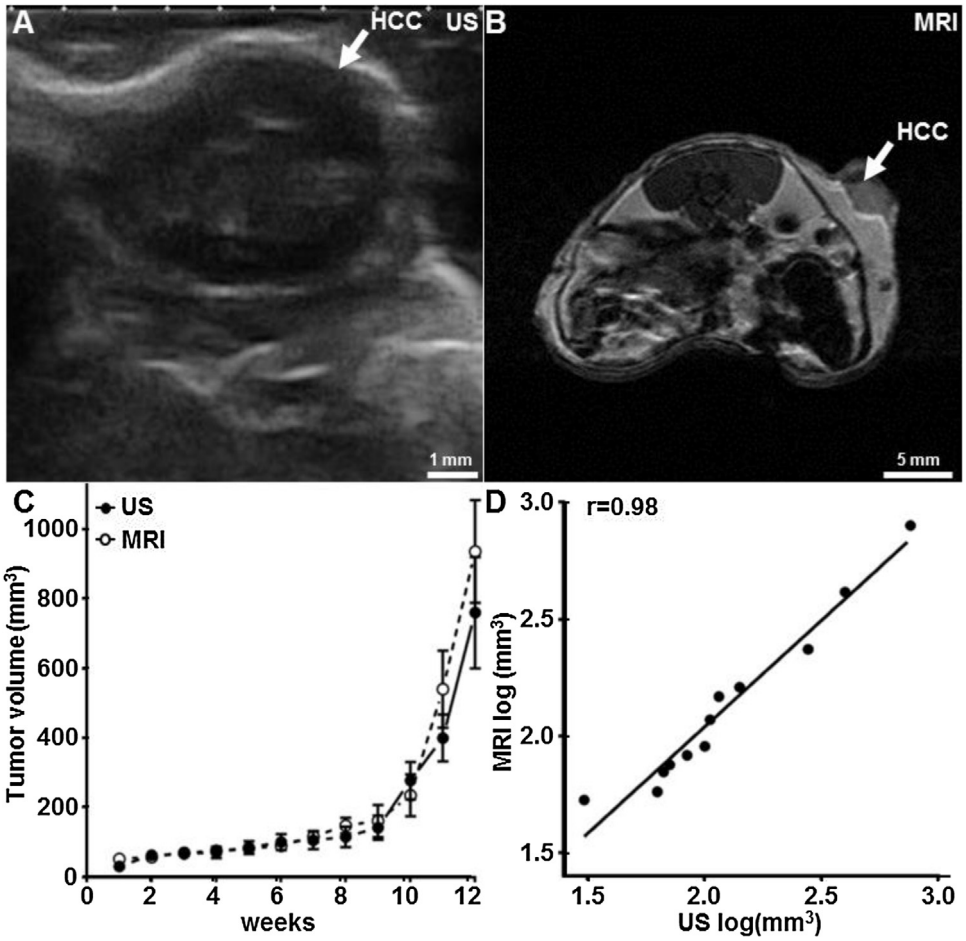


**Fig. 4.** Monitoring of tumor growth. Representative images of subcutaneous HCC tumor (arrow) at 6 weeks post-inoculation are shown with (A) ultrasound (US) and (B) MRI (T1 weighted contrast-enhanced). (C) Mean (±SD) dimensions for n = 8 tumors from US and MRI images from post inoculation weeks 1–12 are shown. (D) Positive correlation of R = 0.98 was found for tumor size measured with US and MRI.

### 3.3. Ultrasound and MRI monitoring of tumor growth

SK-Hep1 cells were inoculated subcutaneously in n = 8 nude mice at 4–6 weeks of age. Tumor size was monitored weekly for 12 weeks. Representative images are shown with ultrasound (US), Fig. 4A, and MRI, Fig. 4B. A peak tumor volume (±SD) of $761 \pm 160$ and $936 \pm 148\,mm^3$ was found on US and MRI, respectively, Fig. 4C. A correlation of R = 0.98 was found between tumor size on US and MRI, Fig. 4D.

### 3.4. Photoacoustic images of HCC xenograft tumor in vivo

At 6 weeks post inoculation, representative photoacoustic images collected with $\lambda_{ex} = 680$ nm at 0, 1, 3, 6, 12, and 24 h after injection of 300 μM in 250 μL of QRH*-Cy5.5 i.v. are shown as maximum intensity projection (MIP) images at a mean (±SD) depth of $8.1 \pm 1.3$ mm with range 0–1.8 cm below the skin surface. At this time, the tumors had reached a mean (±SD) size of $100 \pm 23\,mm^3$ by US. The tumors showed increased signal in a heterogeneous pattern with visible blood vessels, Fig. 5A–F. Preliminary study (data not shown) confirmed wash out of either QRH-Cy5.5 or PEH-Cy5.5 from the animals' system occurred by 24 h post injection and no difference in signal intensity or pattern were associated to injection order. After 48 h when signal was no longer observed from the EGFR peptide, the PEH*-Cy5.5 control peptide was administered in the same animal, Fig. 5G–L. For additional control, images from HCC with Cy5.5 alone, Fig. 5M–R, and from adjacent normal tissue with QRH*-Cy5.5, Fig. 5S, are shown. A volume rendered image of the tumor at 3 h post injection is shown (Video 1), Fig. 5T.

### 3.5. Target-background (T/B) ratio of HCC on photoacoustic images

The photoacoustic intensity from the tumor (target) was measured using a circular ROI with diameter determined from US, and an adjacent annulus with area equal to that of the target ROI was used to measure background (white circles in Fig. 5C). HCC tumors showed a higher T/B ratio for the EGFR peptide compared with that of the control peptide at each time point up to 24 h. Tumor uptake of QRH*-Cy5.5 increased steadily after injection to a peak value at 3 h, Fig. 6A. The T/B ratio then decreased over time to near baseline by 24 h. Meanwhile, non-tumor exhibited minimal uptake. The HCC image with Cy5.5 alone (no peptide) showed a small effect of tumor permeability and retention [37,38]. Injection of Cy5.5 dye alone produced a peak T/B ratio of $1.30 \pm 0.14$ at 1 h post injection at tumor site. We measured a T/B ratio of $1.22 \pm 0.14$ at the tumor site and $1.05 \pm 0.13$ from adjacent normal tissue at 3 h respectively. Peak T/B ratios for the EGFR and control peptides at 3 h are shown, Fig. 6B. The T/B ratios at each time point for individual mice are shown, Fig. S3.

### 3.6. Validation of EGFR peptide binding ex vivo

On immunohistochemistry (IHC), we observed strong staining of EGFR in HCC tumors Fig. 7A. On immunofluorescence (IF), strong signal from QRH*-Cy5.5 is seen on the surface of tumor cells,

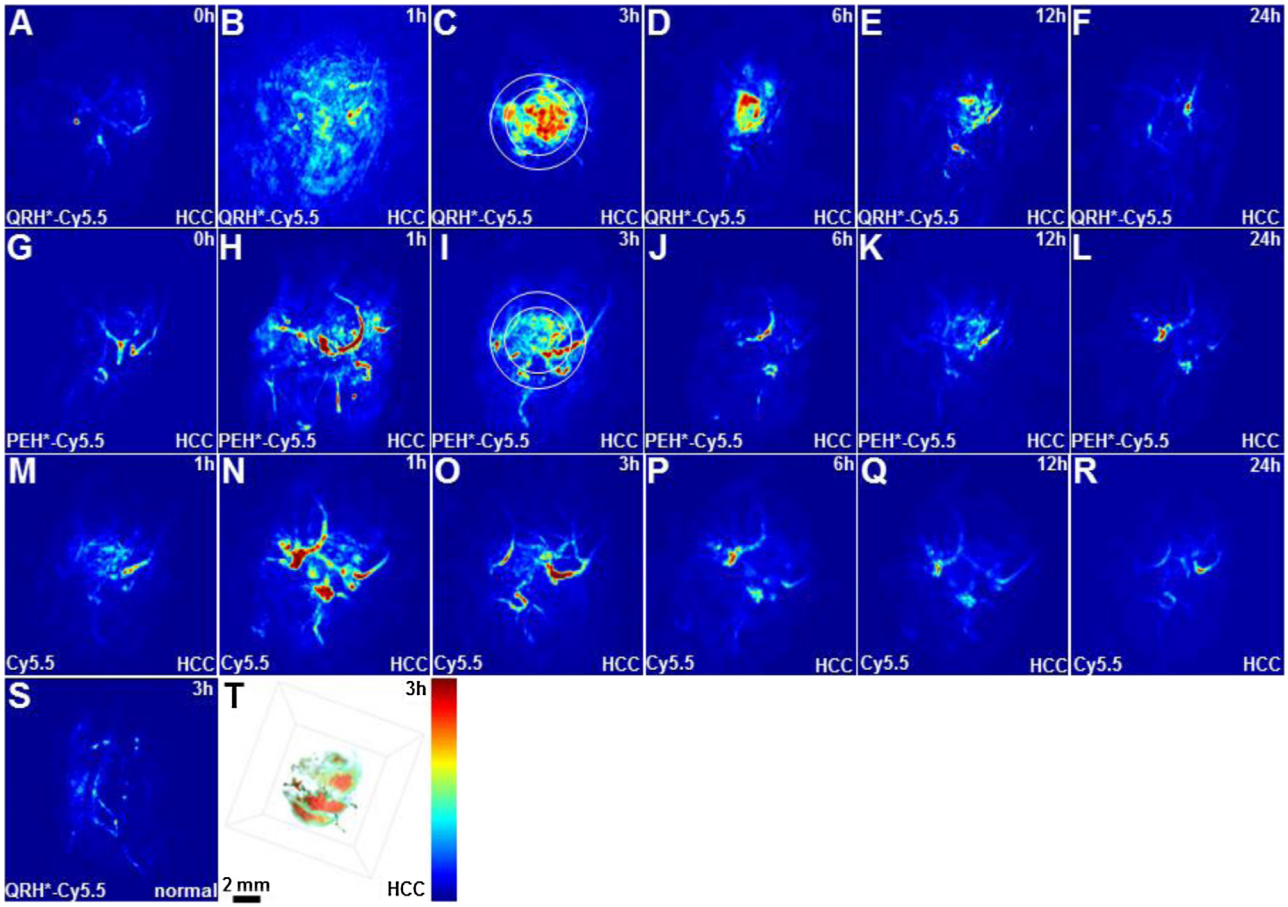


**Fig. 5.** Photoacoustic images of HCC tumor in vivo. Representative MIP images at depth of 1.8 cm were collected at 0, 1, 3, 6, 12 and 24 h after injection with (A–F) QRH*-Cy5.5 and (G–L) PEH*-Cy5.5 are shown. In panel (C), inner circle represents regions-of-interest (ROI) used to measure signal from tumor, and adjacent annulus with equal area was used to measure background. (M–R) Images of tumor with injection of Cy5.5 alone (no peptide) at 0–24 h post injection. (S) Image of normal area at 3 h after QRH-Cy5.5 injection. (T) 3D reconstruction of tumor images.

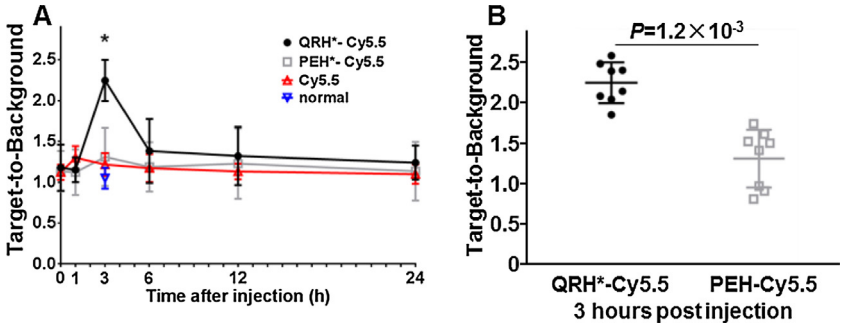


**Fig. 6.** Target-background (T/B) ratio of HCC on photoacoustic images. (A) Images collected over time show peak tumor QRH*-Cy5.5 uptake at 3 h after i.v. injection. T/B ratio of 2.25 ± 0.25 was significantly greater than 1.31 ± 0.36 for PEH*-Cy5.5, $P = 1.2 \times 10^{-3}$ by paired *t*-test. Injection of Cy5.5 dye alone produced peak T/B ratio, 1.30 ± 0.14, at 1 h post injection at tumor site. T/B ratio of 1.22 ± 0.14 at tumor site and 1.05 ± 0.13 at adjacent normal tissue were observed at 3 h respectively. Wash out of probe was observed within 24 h. (B) Individual data points for T/B ratios at 3 h are shown.

Fig. 7B. In normal mouse liver, a few lightly stained hepatocytes (arrow) can be seen surrounding the central vein (arrowhead) with IHC, Fig. 7D. Minimal signal from QRH*-Cy5.5 was seen in normal liver with IF, Fig. 7E. Corresponding histology (H&E) of tumor and normal is shown, Fig. 7C and F. We found the mean fluorescence intensity from HCC to be significantly greater than that of normal

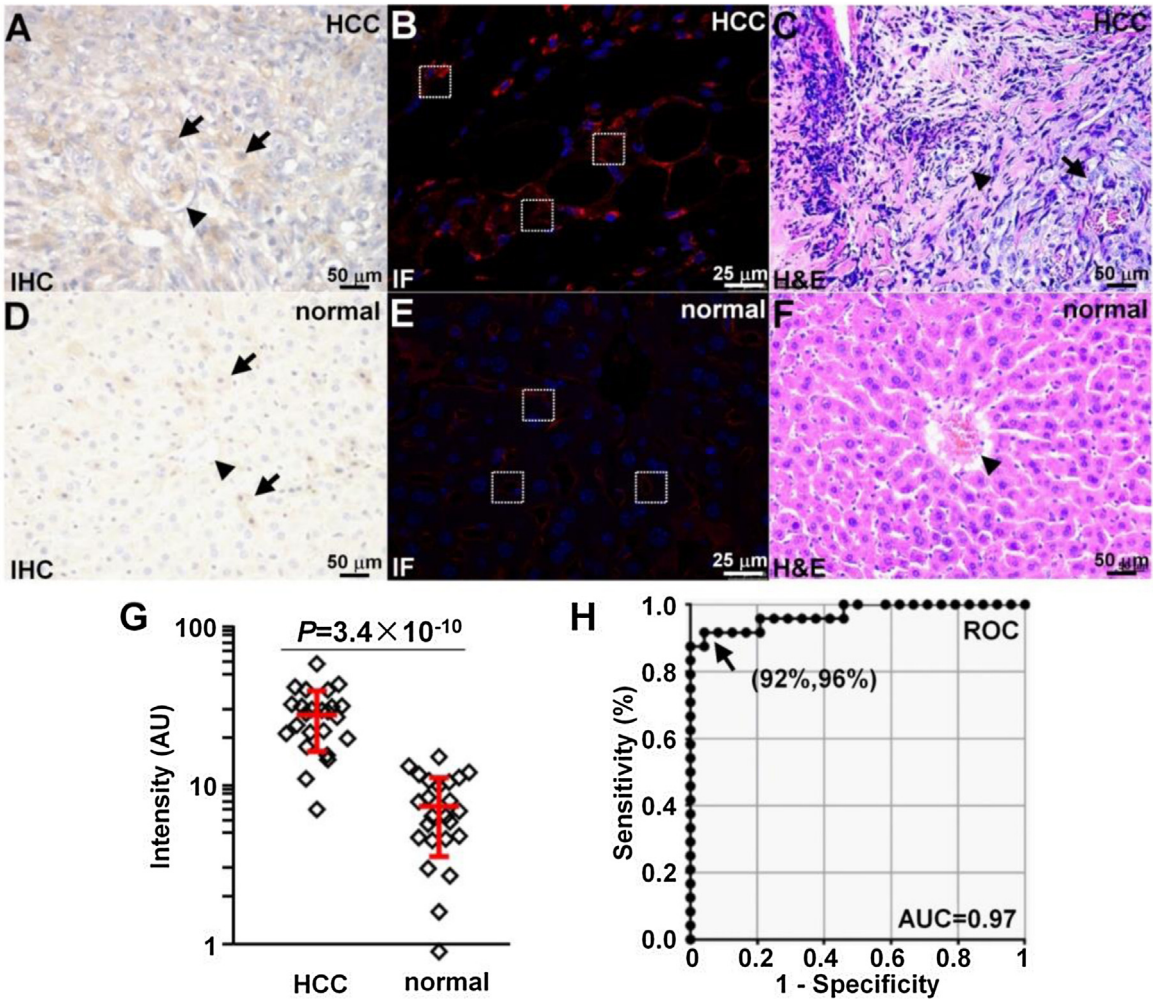


**Fig. 7.** Ex vivo validation of EGFR binding. (A) Immunohistochemistry (IHC) with anti-EGFR antibody shows increased reactivity to HCC. A nest of tumor cells with large irregular round nuclei (arrows) and infiltrating blood vessels lined with flattened endothelial cells (arrowhead) can be seen. (B) Immunofluorescence (IF) with QRH*-Cy5.5 shows binding to surface of HCC cells. Fluorescence intensities were measured from sets of 3 (dashed white) boxes with dimensions of 20 × 20 $\mu m^2$. (C) Corresponding histology (H&E) of tumor. (D) IHC of normal mouse hepatocytes show few lightly stained cells (arrows) surrounding the central vein (arrowhead). (E) IF of normal mouse liver shows minimal signal. (F) Histology of normal mouse liver shows lobule with central vein (arrowhead) surrounded by radially aligned plates of hepatocytes. (G) Mean (±SD) fluorescence intensities for HCC (n = 24 tumors) are significantly higher than that for normal liver (n = 24), 27.8 ± 11.5 versus 7.37 ± 3.80 by 3.77-fold, $P = 3.4 \times 10^{-10}$ by paired *t*-test. (H) ROC curve shows 92% sensitivity and 96% specificity with area under curve (AUC) of 0.97 for distinguishing HCC from normal liver using QRH*-Cy5.5.

by 3.8-fold, Fig. 7G. The corresponding ROC curve shows 92% sensitivity and 96% specificity for distinguishing HCC from normal liver with an area under curve of AUC = 0.97.

## 4. Discussion

Here, we demonstrate use of photoacoustic imaging to visualize HCC xenograft tumors in living mice with a peptide specific for EGFR. This peptide was used previously to collect fluorescence images endoscopically from mouse colonic adenomas with topical administration [31]. We now show that specific binding to EGFR can also occur with systemic administration. We used Cy5.5, a NIR fluorophore, to achieve good photoacoustic signal at a depth down to 1.8 cm with low background. We found peak uptake at 3 h post injection and clearance by ~24 h. This time frame is significantly faster than most antibodies, which can take hours to home to the tumor and even longer to clear [39,40].

Previous photoacoustic imaging studies have used endogenous contrast from hemoglobin and melanin [41], and others have relied on the enhanced permeability and retention (EPR) effect [42,43]. These strategies are based on non-specific detection mechanisms. By comparison, use of a targeting moiety can improve tumor homing, increase signal, and improve contrast by tuning absorption to specific wavelengths [44]. The EPR effect can be variable and produce false positives in highly vascular tissues [37]. Photoacoustic imaging has been used with other molecular probes for targeted detection. An enzyme sensitive oligomer labeled with Atto-740 was used to detect furin-like activity [45]. DMSO was needed to improve solubility, and the oligomers were found to aggregate and form nanostructures that trapped the reporter molecule inside the cells. RGD peptides have been used to target integrins in tumor-associated blood vessels that arise from angiogenesis and metastasis, a finding that occurs at a late stage of tumor development [46–49]. Antibodies labeled with gold nanoparticles have been used to image molecular targets, such as Her-2, EGFR, CXCR4 and LYVE-1 [50–54]. Antibodies are large in size, high in molecular weight, and have long circulatory half-lives [55]. They also have limited ability to extravasate from the vasculature, diffuse within tumors, penetrate deeply, and clear from interstitial space [55,56]. All of these properties increase imaging background. Antibodies are also prone to immunogenicity that limits repetitive use [57].

Epidermal growth factor receptor (EGFR) is overexpressed in many cancers and promotes solid tumor growth [58]. Previous studies have targeted EGFR to improve imaging specificity, and have used metallic nanoparticles [52,54,59] and organic dyes [60–62] to generate contrast. Gold nanospheres [54], gold nanrods [63], silica-coated gold nanorods [64], and silver nanoplates [65] have been labeled with monoclonal EGFR antibodies to image cells overexpressing EGFR [66] with photoacoustic imaging. Targeted nanoparticles can be used as sensors to detect molecular interactions. EGFR-targeted gold nanospheres aggregate in endosomes after undergoing receptor-mediated endocytosis [67]. This results in plasmon coupling and a red shift in the absorption spectrum, which is detectable with photoacoustic imaging. Therefore, nanoparticles in the endosomes of cells overexpressing EGFR can be detected and distinguished from free nanoparticles in the tumor, which may have accumulated via the EPR effect [54]. The high cost and long circulatory time of antibodies as targeting moiety in imaging could potentially inhibit acceptance for clinical translation as a diagnostic tool. This motivates our present study to explore feasibility for use of a cost-efficient and fast acting EGFR targeting peptide.

Photoacoustic imaging is an emerging imaging modality that provides greater depth than optical methods and better resolution than ultrasound. We were able to visualize a large fraction of the volume of HCC tumors, and may be able to improve imaging depth with use of stronger labels, such as nanoparticles [68]. This method may be useful for evaluating the effect of drugs under development for tumor therapy. Previous studies has reported the ability of hybrid plasmonic contrast agent gold nanotube (GNT) to achieve picomolar sensitivity compared to nanomolar levels for conventional agents [36]. Moreover indocyanine green labeled with single walled carbon nanotubes (SWNT-ICG) can improve photoacoustic contrast by ~300-fold [47]. This technique using non-ionizing radiation, and can be more cost-effective and easier to use than MRI, PET, and SPECT. The photoacoustic images were collected with a spatial resolution of 280 μm in all dimensions. By comparison, ultrasound at the same central frequency of 5 MHz without 3D data acquisition and image reconstruction can achieve 470 μm axial and ~1–5 mm lateral resolution [69]. However, high-frequency linear-array-based micro-ultrasound platforms operating at frequencies of 30–70 MHz (compared to frequencies of 3–15 MHz for clinical ultrasound systems) can allow spatial resolution as high as 30-μm [70]. Nuclear imaging methods (PET and SPECT) have spatial resolution in the ~1–2 mm range [44,71]. Our in vivo images required long image acquisition and reconstruction times (~2 min). Faster lasers and more efficient algorithms may enable real time image-guided surgery with a photoacoustic endoscope.

In this study, we used a version of Cy5.5 that has four additional hydrophilic $-SO_3H$ groups (Fig. 1A) to improve water solubility. With the previous fluorophore, we used a concentration of 100 μM, which was adequate for topical administration to detect pre-malignant disease in mouse colon [31]. In this study, we achieved a ~3-fold greater concentration, and used systemic administration to deliver the peptide to a solid tumor. The higher dye solubility allowed for use of a volume that is tolerated by the animal. Because the peak absorption of Cy5.5 occurs below 700 nm, the imaging depth can be improved with organic dyes, such as ICG and Licor IRDye800 [49,72], that absorb at longer wavelengths and avoids hemoglobin absorbance and minimizes tissue scattering. Moreover, nanoparticles have 3–10 times higher extinction coefficient than organic dyes [73], and can absorb more energy from light per mass density. Example of nanoparticles that can be used to label peptides for increased signal include iron oxide [46], gold nanorods [50], CuS [74], nanospheres [54,75], carbon nanotubes [47,76] and polymer nanoparticles [77–80]. Metallic nanoparticles have very strong absorption that can also be used for photothermal therapy after tumor delivery [48,81]. Carbon nanotubes are considered more bio-compatible [82], absorb over a broad spectrum [66], and possess superior photoacoustic signal strengths compared to metallic NPs. Polymer NPs can be more photostable than gold nanorods and photoacoustically brighter than carbon nanotubes with pulsed laser irradiation. Despite these advantages, nanoparticles are foreign bodies that can cause inflammation in liver [83,84] and increase circulation time [85]. While prolonged circulation time of conventional nanoprobes may enhance targeted drug delivery [86,87], peptides may offer advantages for improved deep tumor penetration and accumulation with reduced biodistribution to non-target tissues [88,89]. Among nanomaterial-based agents already approved by the FDA [90], all but one of these agents are therapeutics [91]. On the other hand, nanoparticles have not received FDA approval for clinical imaging [92]. A smart or activatable nanoparticles with improved pharmacokinetic, tumor targeting and organ clearance properties, based on the use of natural, biodegradable polymers (dextran and heparin), is desired. Organic dyes have a benign toxicity profile [93] and pharmacokinetic characteristics are compatible with clinical translation.

The typical shape of tumor xenografts in this study was oblate ellipsoid with almost equal dimensions parallel to skin surface but much shorter in depth beneath the skin (i.e. $b < a \approx c$). Thus

approximation of tumor area with circular ROI was adopted in PA signal intensity measurement for 2D MIP images. 3D volumetric quantification of PA images could potentially give a more accurate intensity measurement if an algorithm capable of defining arbitrary oblate ellipsoid as ROI and taking into account the illumination attenuation along tissue depth were available.

We used human SK-Hep1 cells that overexpress EGFR to introduce HCC xenograft tumors. This technique may produce higher levels of EGFR expression and less heterogeneity than that found in sporadic human HCC [94]. In the future, we will use patient derived xenograft (PDX) models that include stroma and better reflect clinically relevant EGFR expression levels [95] and tumor microenvironment [96]. PDX models can also be effective for evaluating new drugs [97–99]. Both subcutaneous [96,100,101] and orthotopic [102] PDX models of HCC have been developed by other groups. Also, detection of multiple targets simultaneously may be needed to address the genetic diversity of HCC. Our imaging system can use a broad range of wavelengths (680–950 nm). This spectrum covers the absorption peaks of many NIR dyes (Cy5.5, ICG, IRDye800) and nanoparticles (Au, SWNT and Co [50,68,76]). A panel of peptides labeled in spectrally distinct regions may be needed to achieve high detection sensitivity in the clinic. Adapting functionalized nanoparticles for excitation at different wavelengths would allow for multiplexed imaging to be performed [103].

## Conflict of interest

JZ, BPJ, and TDW are co-inventors on a patent application filed by the University of Michigan on the peptide.

## Acknowledgement

Funding was provided in part by National Institutes of Health U54CA163059, U01CA189291, R01 CA142750, R01 CA200007, and R01 EB020644 (T.D.W.) and by Mary L. Petrovich. We thank M. Thornton, P. Picot and T. Morgan from Endra Life Sciences who provided technical training, insight and expertise that greatly assisted the study.

## Appendix A. Supplementary data

Supplementary data associated with this article can be found, in the online version, at http://dx.doi.org/10.1016/j.pacs.2016.04.001.

## References

[1] J. Ferlay, I. Soerjomataram, R. Dikshit, S. Eser, C. Mathers, M. Rebelo, et al., Cancer incidence and mortality worldwide: sources, methods and major patterns in GLOBOCAN 2012, Int. J. Cancer 136 (2015) E359–E386, doi:http://dx.doi.org/10.1002/ijc.29210.
[2] M. Kudo, Hepatocellular carcinoma 2009 and beyond: from the surveillance to molecular targeted therapy, Oncology 75 (Suppl. 1) (2008) 1–12, doi:http://dx.doi.org/10.1159/000181865.
[3] M. Maluccio, A. Covey, Recent progress in understanding, diagnosing, and treating hepatocellular carcinoma, CA Cancer J. Clin. 62 (2012) 394–399, doi:http://dx.doi.org/10.3322/caac.21161.
[4] S.A. Shah, S.P. Cleary, A.C. Wei, I. Yang, B.R. Taylor, A.W. Hemming, et al., Recurrence after liver resection for hepatocellular carcinoma: risk factors, treatment, and outcomes, Surgery 141 (2007) 330–339, doi:http://dx.doi.org/10.1016/j.surg.2006.06.028.
[5] M. Capurro, I.R. Wanless, M. Sherman, G. Deboer, W. Shi, E. Miyoshi, et al., Glypican-3: a novel serum and histochemical marker for hepatocellular carcinoma, Gastroenterology 125 (2003) 89–97, doi:http://dx.doi.org/10.1016/S0016-5085(03)00689-9.
[6] J. Bruix, M. Sherman, Management of hepatocellular carcinoma, Hepatology 42 (2005) 1208–1236, doi:http://dx.doi.org/10.1002/hep.20933.
[7] N.N. Massarweh, J.O. Park, F. Farjah, R.S. Yeung, R.G. Symons, T.L. Vaughan, et al., Trends in the utilization and impact of radiofrequency ablation for hepatocellular carcinoma, J. Am. Coll. Surg. 210 (2010) 441–448, doi:http://dx.doi.org/10.1016/j.jamcollsurg.2009.12.026.
[8] L. Bolondi, Surveillance programme of cirrhotic patients for early diagnosis and treatment of hepatocellular carcinoma: a cost effectiveness analysis, Gut 48 (2001) 251–259, doi:http://dx.doi.org/10.1136/gut.48.2.251.
[9] G. Fattovich, T. Stroffolini, I. Zagni, F. Donato, Hepatocellular carcinoma in cirrhosis: incidence and risk factors, Gastroenterology 127 (2004) S35–S50. http://www.ncbi.nlm.nih.gov/ubmed/15508101.
[10] A. Sangiovanni, E. Del Ninno, P. Fasani, C. De Fazio, G. Ronchi, R. Romeo, et al., Increased survival of cirrhotic patients with a hepatocellular carcinoma detected during surveillance, Gastroenterology 126 (2004) 1005–1014, doi:http://dx.doi.org/10.1053/j.gastro.2003.12.049.
[11] H. Masuda, D. Zhang, C. Bartholomeusz, H. Doihara, G.N. Hortobagyi, N.T. Ueno, Role of epidermal growth factor receptor in breast cancer, Breast Cancer Res. Treat. 136 (2012) 331–345, doi:http://dx.doi.org/10.1007/s10549-012-2289-9.
[12] T. Troiani, E. Martinelli, A. Capasso, F. Morgillo, M. Orditura, F. De Vita, et al., Targeting EGFR in pancreatic cancer treatment, Curr. Drug Targets 13 (2012) 802–810, doi:http://dx.doi.org/10.2174/138945012800564158.
[13] M.D. Siegelin, A.C. Borczuk, Epidermal growth factor receptor mutations in lung adenocarcinoma, Lab. Investig. 94 (2014) 129–137, doi:http://dx.doi.org/10.1038/labinvest.2013.147.
[14] Y. Ito, T. Takeda, M. Sakon, M. Tsujimoto, S. Higashiyama, K. Noda, et al., Expression and clinical significance of erb-B receptor family in hepatocellular carcinoma, Br. J. Cancer 84 (2001) 1377–1383, doi:http://dx.doi.org/10.1054/bjoc.2000.1580.
[15] E. Schiffer, C. Housset, W. Cacheux, D. Wendum, C. Desbois-Mouthon, C. Rey, et al., Gefitinib, an EGFR inhibitor, prevents hepatocellular carcinoma development in the rat liver with cirrhosis, Hepatology 41 (2005) 307–314, doi:http://dx.doi.org/10.1002/hep.20538.
[16] A. El-Bassiouni, M. Nosseir, M. Zoheiry, E. El-Ahwany, A. Ghali, N. El-Bassiouni, Immunohistochemical expression of CD95 (Fas), c-myc and epidermal growth factor receptor in hepatitis C virus infection, cirrhotic liver disease and hepatocellular carcinoma, APMIS 114 (2006) 420–427, doi:http://dx.doi.org/10.1111/j.1600-0463.2006.apm_323.x.
[17] A.F. Buckley, L.J. Burgart, V. Sahai, S. Kakar, Epidermal growth factor receptor expression and gene copy number in conventional hepatocellular carcinoma, Am. J. Clin. Pathol. 129 (2008) 245–251, doi:http://dx.doi.org/10.1309/WF10QAAED3PP93BH.
[18] C. Berasain, M. Ujue Latasa, R. Urtasun, S. Goni, M. Elizalde, O. Garcia-Irigoyen, et al., Epidermal growth factor receptor (EGFR) crosstalks in liver cancer, Cancers (Basel) 3 (2011) 2444–2461, doi:http://dx.doi.org/10.3390/cancers3022444.
[19] N. Yoneda, Y. Sato, A. Kitao, H. Ikeda, S. Sawada-Kitamura, M. Miyakoshi, et al., Epidermal growth factor induces cytokeratin 19 expression accompanied by increased growth abilities in human hepatocellular carcinoma, Lab. Investig. 91 (2011) 262–272, doi:http://dx.doi.org/10.1038/labinvest.2010.161.
[20] M. Höpfner, A.P. Sutter, A. Huether, D. Schuppan, M. Zeitz, H. Scherübl, Targeting the epidermal growth factor receptor by gefitinib for treatment of hepatocellular carcinoma, J. Hepatol. 41 (2004) 1008–1016, doi:http://dx.doi.org/10.1016/j.jhep.2004.08.024.
[21] S. Uslu, H. Kirimlioglu, U. Ince, Analysis of epidermal growth factor receptor expression in hepatocellular carcinoma: a comparision of fluorescence in situ hybridization and immunochemistry, J. Gastroenterol. Hepatol. Res. 3 (2014) 1193–1197, doi:http://dx.doi.org/10.6051/j.issn.2224-3992.2014.03.448.
[22] M. Matsuo, H. Sakurai, I. Saiki, ZD1839, a selective epidermal growth factor receptor tyrosine kinase inhibitor, shows antimetastatic activity using a hepatocellular carcinoma model, Mol. Cancer Ther. 2 (2003) 557–561. http://www.ncbi.nlm.nih.gov/pubmed/12813135.
[23] H.-W. Lo, S.-C. Hsu, W. Xia, X. Cao, J.-Y. Shih, Y. Wei, et al., Epidermal growth factor receptor cooperates with signal transducer and activator of transcription 3 to induce epithelial-mesenchymal transition in cancer cells via up-regulation of TWIST gene expression, Cancer Res. 67 (2007) 9066–9076, doi:http://dx.doi.org/10.1158/0008-5472.CAN-07-0575.
[24] J. Lupberger, M.B. Zeisel, F. Xiao, C. Thumann, I. Fofana, L. Zona, et al., EGFR and EphA2 are host factors for hepatitis C virus entry and possible targets for antiviral therapy, Nat. Med. 17 (2011) 589–595, doi:http://dx.doi.org/10.1038/nm.2341.
[25] F.R. Hirsch, Epidermal growth factor receptor in non-small-cell lung carcinomas: correlation between gene copy number and protein expression and impact on prognosis, J. Clin. Oncol. 21 (2003) 3798–3807, doi:http://dx.doi.org/10.1200/JCO.2003.11.069.
[26] R. Bhargava, W.L. Gerald, A.R. Li, Q. Pan, P. Lal, M. Ladanyi, et al., EGFR gene amplification in breast cancer: correlation with epidermal growth factor receptor mRNA and protein expression and HER-2 status and absence of EGFR-activating mutations, Mod. Pathol. 18 (2005) 1027–1033, doi:http://dx.doi.org/10.1038/modpathol.3800438.
[27] A. Jimeno, A.C. Tan, J. Coffa, N.V. Rajeshkumar, P. Kulesza, B. Rubio-Viqueira, et al., Coordinated epidermal growth factor receptor pathway gene overexpression predicts epidermal growth factor receptor inhibitor sensitivity in pancreatic cancer, Cancer Res. 68 (2008) 2841–2849, doi:http://dx.doi.org/10.1158/0008-5472.CAN-07-5200.
[28] C.W. Reuter, M.A. Morgan, A. Eckardt, Targeting EGF-receptor-signalling in squamous cell carcinomas of the head and neck, Br. J. Cancer 96 (2007) 408–416, doi:http://dx.doi.org/10.1038/sj.bjc.6603566.
[29] M. Hanawa, S. Suzuki, Y. Dobashi, T. Yamane, K. Kono, N. Enomoto, et al., EGFR protein overexpression and gene amplification in squamous cell carcinomas

of the esophagus, Int. J. Cancer 118 (2006) 1173–1180, doi:http://dx.doi.org/10.1002/ijc.21454.
[30] P. Zhao, X. Yang, S. Qi, H. Liu, H. Jiang, S. Hoppmann, et al., Molecular imaging of hepatocellular carcinoma xenografts with epidermal growth factor receptor targeted affibody probes, Biomed. Res. Int. 2013 (2013) 759057, doi:http://dx.doi.org/10.1155/2013/759057.
[31] J. Zhou, B.P. Joshi, X. Duan, A. Pant, Z. Qiu, R. Kuick, et al., EGFR overexpressed in colonic neoplasia can be detected on wide-field endoscopic imaging, Clin. Transl. Gastroenterol. 6 (2015) e101, doi:http://dx.doi.org/10.1038/ctg.2015.28.
[32] H.-J. Wester, H. Kessler, Molecular targeting with peptides or peptide-polymer conjugates: just a question of size? J. Nucl. Med. 46 (2005) 1940–1945. http://www.ncbi.nlm.nih.gov/pubmed/16330555.
[33] S. Lee, J. Xie, X. Chen, Peptides and peptide hormones for molecular imaging and disease diagnosis, Chem. Rev. 110 (2010) 3087–3111, doi:http://dx.doi.org/10.1021/cr900361p.
[34] G.D. Ayers, E.T. McKinley, P. Zhao, J.M. Fritz, R.E. Metry, B.C. Deal, et al., Volume of preclinical xenograft tumors is more accurately assessed by ultrasound imaging than manual caliper measurements, J. Ultrasound Med. 29 (2010) 891–901. http://www.ncbi.nlm.nih.gov/pubmed/20498463.
[35] K.C. Graham, L.A. Wirtzfeld, L.T. MacKenzie, C.O. Postenka, A.C. Groom, I.C. MacDonald, et al., Three-dimensional high-frequency ultrasound imaging for longitudinal evaluation of liver metastases in preclinical models, Cancer Res. 65 (2005) 5231–5237, doi:http://dx.doi.org/10.1158/0008-5472.CAN-05-0440.
[36] D. Kruger, G. Reinecke, M. Kruger, P. Thornton, et al., HYPR-spectral photoacoustic CT for preclinical imaging, in: A.A. Oraevsky, L.V. Wang (Eds.), SPIE BiOS Biomedical Optics, International Society for Optics and Photonics, 2009, pp. 71770F, doi:http://dx.doi.org/10.1117/12.810175.
[37] H. Maeda, J. Wu, T. Sawa, Y. Matsumura, K. Hori, Tumor vascular permeability and the EPR effect in macromolecular therapeutics: a review, J. Control. Release 65 (2000) 271–284, doi:http://dx.doi.org/10.1016/S0168-3659(99)00248-5.
[38] A.K. Iyer, G. Khaled, J. Fang, H. Maeda, Exploiting the enhanced permeability and retention effect for tumor targeting, Drug Discov. Today 11 (2006) 812–818, doi:http://dx.doi.org/10.1016/j.drudis.2006.07.005.
[39] L. Yang, H. Mao, Y.A. Wang, Z. Cao, X. Peng, X. Wang, et al., Single chain epidermal growth factor receptor antibody conjugated nanoparticles for in vivo tumor targeting and imaging, Small 5 (2008) 235–243, doi:http://dx.doi.org/10.1002/smll.200800714.
[40] H.S.T. Cao, S. Kaushal, C.A. Metildi, R.S. Menen, C. Lee, C.S. Snyder, et al., Tumor-specific fluorescence antibody imaging enables accurate staging laparoscopy in an orthotopic model of pancreatic cancer, Hepatogastroenterology 59 (2011) 1994, doi:http://dx.doi.org/10.5754/hge11836.
[41] H.F. Zhang, K. Maslov, G. Stoica, L.V. Wang, Functional photoacoustic microscopy for high-resolution and noninvasive in vivo imaging, Nat. Biotechnol. 24 (2006) 848–851, doi:http://dx.doi.org/10.1038/nbt1220.
[42] Y. Wang, X. Xie, X. Wang, G. Ku, K.L. Gill, D.P. O'Neal, et al., Photoacoustic tomography of a nanoshell contrast agent in the in vivo rat brain, Nano Lett. 4 (2004) 1689–1692, doi:http://dx.doi.org/10.1021/nl049126a.
[43] Q. Zhang, N. Iwakuma, P. Sharma, B.M. Moudgil, C. Wu, J. McNeill, et al., Gold nanoparticles as a contrast agent for in vivo tumor imaging with photoacoustic tomography, Nanotechnology 20 (2009) 395102, doi:http://dx.doi.org/10.1088/0957-4484/20/39/395102.
[44] S. Mallidi, G.P. Luke, S. Emelianov, Photoacoustic imaging in cancer detection, diagnosis, and treatment guidance, Trends Biotechnol. 29 (2011) 213–221.
[45] A. Dragulescu-Andrasi, S.-R. Kothapalli, G.A. Tikhomirov, J. Rao, S.S. Gambhir, Activatable oligomerizable imaging agents for photoacoustic imaging of furin-like activity in living subjects, J. Am. Chem. Soc. 135 (2013) 11015–11022, doi:http://dx.doi.org/10.1021/ja4010078.
[46] K. Chen, J. Xie, H. Xu, D. Behera, M.H. Michalski, S. Biswal, et al., Triblock copolymer coated iron oxide nanoparticle conjugate for tumor integrin targeting, Biomaterials 30 (2009) 6912–6919, doi:http://dx.doi.org/10.1016/j.biomaterials.2009.08.045.
[47] A. de la Zerda, Z. Liu, S. Bodapati, R. Teed, S. Vaithilingam, B.T. Khuri-Yakub, et al., Ultrahigh sensitivity carbon nanotube agents for photoacoustic molecular imaging in living mice, Nano Lett. 10 (2010) 2168–2172, doi:http://dx.doi.org/10.1021/nl100890d.
[48] W. Lu, M.P. Melancon, C. Xiong, Q. Huang, A. Elliott, S. Song, et al., Effects of photoacoustic imaging and photothermal ablation therapy mediated by targeted hollow gold nanospheres in an orthotopic mouse xenograft model of glioma, Cancer Res. 71 (2011) 6116–6121, doi:http://dx.doi.org/10.1158/0008-5472.CAN-10-4557.
[49] M.-L. Li, J.-T. Oh, X. Xie, G. Ku, W. Wang, C. Li, et al., Simultaneous molecular and hypoxia imaging of brain tumors in vivo using spectroscopic photoacoustic tomography, Proc. IEEE 96 (2008) 481–489, doi:http://dx.doi.org/10.1109/JPROC.2007.913515.
[50] A. Agarwal, S.W. Huang, M. O'Donnell, K.C. Day, M. Day, N. Kotov, et al., Targeted gold nanorod contrast agent for prostate cancer detection by photoacoustic imaging, J. Appl. Phys. 102 (2007) 64701, doi:http://dx.doi.org/10.1063/1.2777127.
[51] P.-C. Li, C.-W. Wei, C.-K. Liao, C.-D. Chen, K.-C. Pao, C.-R.C. Wang, et al., Photoacoustic imaging of multiple targets using gold nanorods, IEEE Trans. Ultrason. Ferroelectr. Freq. Control 54 (2007) 1642–1647, doi:http://dx.doi.org/10.1109/TUFFC.2007.435.
[52] P.-C. Li, C.-R.C. Wang, D.-B. Shieh, C.-W. Wei, C.-K. Liao, C. Poe, et al., In vivo photoacoustic molecular imaging with simultaneous multiple selective targeting using antibody-conjugated gold nanorods, Opt. Express 16 (2008) 18605, doi:http://dx.doi.org/10.1364/oe.16.018605.
[53] J.-W. Kim, E.I. Galanzha, E.V. Shashkov, H.-M. Moon, V.P. Zharov, Golden carbon nanotubes as multimodal photoacoustic and photothermal high-contrast molecular agents, Nat. Nanotechnol. 4 (2009) 688–694, doi:http://dx.doi.org/10.1038/nnano.2009.231.
[54] S. Mallidi, T. Larson, J. Tam, P.P. Joshi, A. Karpiouk, K. Sokolov, et al., Multiwavelength photoacoustic imaging and plasmon resonance coupling of gold nanoparticles for selective detection of cancer, Nano Lett. 9 (2009) 2825–2831, doi:http://dx.doi.org/10.1021/nl802929u.
[55] P.M. Glassman, J.P. Balthasar, Mechanistic considerations for the use of monoclonal antibodies for cancer therapy, Cancer Biol. Med. 11 (2014) 20–33, doi:http://dx.doi.org/10.7497/j.issn.2095-3941.2014.01.002.
[56] W. Wang, E. Wang, J. Balthasar, Monoclonal antibody pharmacokinetics and pharmacodynamics, Clin. Pharmacol. Ther. 84 (2008) 548–558, doi:http://dx.doi.org/10.1038/clpt.2008.170.
[57] F.A. Harding, M.M. Stickler, J. Razo, R. DuBridge, The immunogenicity of humanized and fully human antibodies, MAbs 2 (2010) 256–265, doi:http://dx.doi.org/10.4161/mabs.2.3.11641.
[58] R.I. Nicholson, J.M.W. Gee, M.E. Harper, EGFR and cancer prognosis, Eur. J. Cancer 37 (2001) 9–15, doi:http://dx.doi.org/10.1016/S0959-8049(01)00231-3.
[59] S. Mallidi, P.P. Joshi, K. Sokolov, S. Emelianov, On sensitivity of molecular specific photoacoustic imaging using plasmonic gold nanoparticles, Annual International Conference of the IEEE Engineering in Medicine and Biology Society, IEEE (2009) 6338–6340, doi:http://dx.doi.org/10.1109/IEMBS.2009.5333161.
[60] S. Ke, X. Wen, M. Gurfinkel, C. Charnsangavej, S. Wallace, E.M. Sevick-Muraca, et al., Near-infrared optical imaging of epidermal growth factor receptor in breast cancer xenografts, Cancer Res. 63 (2003) 7870–7875 PMID: 14633715.
[61] N. Nitin, K.J. Rosbach, A. El-Naggar, M. Williams, A. Gillenwater, R.R. Richards-Kortum, Optical molecular imaging of epidermal growth factor receptor expression to improve detection of oral neoplasia, Neoplasia 11 (2009) 542–551, doi:http://dx.doi.org/10.1593/neo.09188.
[62] S.V. Hudson, J.S. Huang, W. Yin, S. Albeituni, J. Rush, A. Khanal, et al., Targeted noninvasive imaging of EGFR-expressing orthotopic pancreatic cancer using multispectral optoacoustic tomography, Cancer Res. 74 (2014) 6271–6279, doi:http://dx.doi.org/10.1158/0008-5472.CAN-14-1656.
[63] A.J. Shah, E.J. Alles, C. Box, S.A. Eccles, S.P. Robinson, J.C. Bamber, Non-invasive molecular profiling of cancer using photoacoustic imaging of functionalized gold nanorods, SPIE BiOS, International Society for Optics and Photonics, 2014, doi:http://dx.doi.org/10.1117/12.2038412 p. 89435G–89435G-10.
[64] C.L. Bayer, Y.-S. Chen, S. Kim, S. Mallidi, K. Sokolov, S. Emelianov, Multiplex photoacoustic molecular imaging using targeted silica-coated gold nanorods, Biomed. Opt. Express 2 (2011) 1828–1835, doi:http://dx.doi.org/10.1364/BOE.2.001828.
[65] K.A. Homan, M. Souza, R. Truby, G.P. Luke, C. Green, E. Vreeland, et al., Silver nanoplate contrast agents for in vivo molecular photoacoustic imaging, ACS Nano 6 (2012) 641–650, doi:http://dx.doi.org/10.1021/nn204100n.
[66] G.P. Luke, D. Yeager, S.Y. Emelianov, Biomedical applications of photoacoustic imaging with exogenous contrast agents, Ann. Biomed. Eng. 40 (2012) 422–437, doi:http://dx.doi.org/10.1007/s10439-011-0449-4.
[67] K. Sokolov, M. Follen, J. Aaron, I. Pavlova, A. Malpica, R. Lotan, et al., Real-time vital optical imaging of precancer using anti-epidermal growth factor receptor antibodies conjugated to gold nanoparticles, Cancer Res. 63 (2003) 1999–2004 PMID: 12727808.
[68] L. Bouchard, M.S. Anwar, G.L. Liu, B. Hann, Z.H. Xie, J.W. Gray, et al., Picomolar sensitivity MRI and photoacoustic imaging of cobalt nanoparticles, Proc. Natl. Acad. Sci. U. S. A. 106 (2009) 4085–4089, doi:http://dx.doi.org/10.1073/pnas.0813019106.
[69] B.C. Albensi, E.V. Ilkanich, G. Dini, D. Janigro, Elements of scientific visualization in basic neuroscience research, Bioscience 54 (2004) 1127, doi:http://dx.doi.org/10.1641/0006-3568(2004)054[1127:EOSVIB]2.0.CO;2.
[70] M. Lakshman, A. Needles, Screening and quantification of the tumor microenvironment with micro-ultrasound and photoacoustic imaging, Nat. Methods 12 (2015), doi:http://dx.doi.org/10.1038/nmeth.f.381.
[71] M.M. Khalil, J.L. Tremoleda, T.B. Bayomy, W. Gsell, Molecular SPECT imaging: an overview, Int. J. Mol. Imaging 2011 (2011) 796025, doi:http://dx.doi.org/10.1155/2011/796025.
[72] S. Zanganeh, H. Li, P.D. Kumavor, U. Alqasemi, A. Aguirre, I. Mohammad, et al., Photoacoustic imaging enhanced by indocyanine green-conjugated single-wall carbon nanotubes, J. Biomed. Opt. 18 (2013) 096006, doi:http://dx.doi.org/10.1117/1.JBO.18.9.096006.
[73] P.K. Jain, K.S. Lee, I.H. El-Sayed, M.A. El-Sayed, Calculated absorption and scattering properties of gold nanoparticles of different size, shape, and composition: applications in biological imaging and biomedicine, J. Phys. Chem. B 110 (2006) 7238–7248, doi:http://dx.doi.org/10.1021/jp057170o.
[74] G. Ku, M. Zhou, S. Song, Q. Huang, J. Hazle, C. Li, Copper sulfide nanoparticles as a new class of photoacoustic contrast agent for deep tissue imaging at 1064 nm, ACS Nano 6 (2012) 7489–7496, doi:http://dx.doi.org/10.1021/nn302782y.
[75] X. Yang, E.W. Stein, S. Ashkenazi, L.V. Wang, Nanoparticles for photoacoustic imaging, Wiley Interdiscip. Rev. Nanomed. Nanobiotechnol. 1 (2009) 360–368, doi:http://dx.doi.org/10.1002/wnan.42.

[76] A. De la Zerda, C. Zavaleta, S. Keren, S. Vaithilingam, S. Bodapati, Z. Liu, et al., Carbon nanotubes as photoacoustic molecular imaging agents in living mice, Nat. Nanotechnol. 3 (2008) 557–562, doi:http://dx.doi.org/10.1038/nnano.2008.231.
[77] K. Pu, A.J. Shuhendler, J. Rao, Semiconducting polymer nanoprobe for in vivo imaging of reactive oxygen and nitrogen species, Angew. Chem. Int. Ed. 52 (2013) 10325–10329, doi:http://dx.doi.org/10.1002/anie.201303420.
[78] K. Pu, A.J. Shuhendler, J.V. Jokerst, J. Mei, S.S. Gambhir, Z. Bao, et al., Semiconducting polymer nanoparticles as photoacoustic molecular imaging probes in living mice, Nat. Nanotechnol. 9 (2014) 233–239, doi:http://dx.doi.org/10.1038/nnano.2013.302.
[79] J. Liu, J. Geng, L.-D. Liao, N. Thakor, X. Gao, B. Liu, Conjugated polymer nanoparticles for photoacoustic vascular imaging, Polym. Chem. 5 (2014) 2854–2862, doi:http://dx.doi.org/10.1039/c3py01587d.
[80] K. Pu, J. Mei, J.V. Jokerst, G. Hong, A.L. Antaris, N. Chattopadhyay, et al., Diketopyrrolopyrrole-based semiconducting polymer nanoparticles for in vivo photoacoustic imaging, Adv. Mater. 27 (2015) 5184–5190, doi:http://dx.doi.org/10.1002/adma.201502285.
[81] R.R. Letfullin, C. Joenathan, T.F. George, V.P. Zharov, Laser-induced explosion of gold nanoparticles: potential role for nanophotothermolysis of cancer, Nanomedicine 1 (2006) 473–480, doi:http://dx.doi.org/10.2217/17435889.1.4.473.
[82] Z. Liu, W. Cai, L. He, N. Nakayama, K. Chen, X. Sun, et al., In vivo biodistribution and highly efficient tumour targeting of carbon nanotubes in mice, Nat. Nanotechnol. 2 (2007) 47–52, doi:http://dx.doi.org/10.1038/nnano.2006.170.
[83] W.S. Cho, M. Cho, J. Jeong, M. Choi, H.Y. Cho, B.S. Han, et al., Acute toxicity and pharmacokinetics of 13 nm-sized PEG-coated gold nanoparticles, Toxicol. Appl. Pharmacol. 236 (2009) 16–24, doi:http://dx.doi.org/10.1016/j.taap.2008.12.023.
[84] E.C. Cho, J. Xie, P.A. Wurm, Y. Xia, Understanding the role of surface charges in cellular adsorption versus internalization by selectively removing gold nanoparticles on the cell surface with a I2/KI etchant, Nano Lett. 9 (2009) 1080–1084, doi:http://dx.doi.org/10.1021/nl803487r.
[86] T. Niidome, M. Yamagata, Y. Okamoto, Y. Akiyama, H. Takahashi, T. Kawano, et al., PEG-modified gold nanorods with a stealth character for in vivo applications, J. Control. Release 114 (2006) 343–347, doi:http://dx.doi.org/10.1016/j.jconrel.2006.06.017.
[87] J.-W. Yoo, E. Chambers, S. Mitragotri, Factors that control the circulation time of nanoparticles in blood: challenges, solutions and future prospects, Curr. Pharm. Des. 16 (2010) 2298–2307, doi:http://dx.doi.org/10.2174/138161210791920496.
[88] H.S. Choi, W. Liu, P. Misra, E. Tanaka, J.P. Zimmer, B.I. Ipe, et al., Renal clearance of quantum dots, Nat. Biotechnol. 25 (2007) 1165–1170, doi:http://dx.doi.org/10.1038/nbt1340.
[89] M. Yu, J. Zheng, Clearance pathways and tumor targeting of imaging nanoparticles, ACS Nano 9 (2015) 6655–6674, doi:http://dx.doi.org/10.1021/acsnano.5b01320.
[90] G. Pillai, Nanomedicines for cancer therapy: an update of FDA approved and those under various stages of development, SOJ Pharm. Pharm. Sci. 1 (2014) 13, doi:http://dx.doi.org/10.15226/2374-6866/1/2/00109.
[91] H.S. Choi, J.V. Frangioni, Nanoparticles for biomedical imaging: fundamentals of clinical translation, Mol. Imaging 9 (2010) 291–310, doi:http://dx.doi.org/10.2310/7290.2010.00031.
[92] M.S. Murahari, M.C. Yergeri, Identification and usage of fluorescent probes as nanoparticle contrast agents in detecting cancer, Curr. Pharm. Des. 19 (2013) 4622–4640, doi:http://dx.doi.org/10.2174/1381612811319250009.
[93] R. Alford, H.M. Simpson, J. Duberman, G.C. Hill, M. Ogawa, C. Regino, et al., Toxicity of organic fluorophores used in molecular imaging: literature review, Mol. Imaging 8 (2009) 341, doi:http://dx.doi.org/10.2310/7290.2009.00031.
[94] E. Fransvea, A. Paradiso, S. Antonaci, G. Giannelli, HCC heterogeneity: molecular pathogenesis and clinical implications, Cell. Oncol. 31 (2009) 227–233, doi:http://dx.doi.org/10.3233/CLO-2009-0473.
[95] T. Yamashita, J. Ji, A. Budhu, M. Forgues, W. Yang, H. Wang, et al., EpCAM-positive hepatocellular carcinoma cells are tumor-Initiating cells with stem/progenitor cell features, Gastroenterology 136 (2009) 1012–1024, doi:http://dx.doi.org/10.1053/j.gastro.2008.12.004 e4.
[96] H. Huynh, K.H. Pierce Chow, K.C. Soo, H.C. Toh, S.P. Choo, K.F. Foo, et al., RAD001 (everolimus) inhibits tumour growth in xenograft models of human hepatocellular carcinoma, J. Cell. Mol. Med. 13 (2009) 1371–1380, doi:http://dx.doi.org/10.1111/j.1582-4934.2008.00364.x.
[97] E. Marangoni, A. Vincent-Salomon, N. Auger, A. Degeorges, F. Assayag, P. de Cremoux, et al., A new model of patient tumor-derived breast cancer xenografts for preclinical assays, Clin. Cancer Res. 13 (2007) 3989–3998, doi:http://dx.doi.org/10.1158/1078-0432.CCR-07-0078.
[98] X. Dong, J. Guan, J.C. English, J. Flint, J. Yee, K. Evans, et al., Patient-derived first generation xenografts of non-small cell lung cancers: promising tools for predicting drug responses for personalized chemotherapy, Clin. Cancer Res. 16 (2010) 1442–1451, doi:http://dx.doi.org/10.1158/1078-0432.CCR-09-2878.
[99] J.J. Tentler, A.C. Tan, C.D. Weekes, A. Jimeno, S. Leong, T.M. Pitts, et al., Patient-derived tumour xenografts as models for oncology drug development, Nat. Rev. Clin. Oncol. 9 (2012) 338–350, doi:http://dx.doi.org/10.1038/nrclinonc.2012.61.
[100] H. Huynh, Xenografts of human hepatocellular carcinoma: a useful model for testing drugs, Clin. Cancer Res. 12 (2006) 4306–4314, doi:http://dx.doi.org/10.1158/1078-0432.CCR-05-2568.
[101] H. Huynh, V.C. Ngo, J. Fargnoli, M. Ayers, K.C. Soo, H.N. Koong, et al., Brivanib alaninate, a dual inhibitor of vascular endothelial growth factor receptor and fibroblast growth factor receptor tyrosine kinases induces growth inhibition in mouse models of human hepatocellular carcinoma, Clin. Cancer Res. 14 (2008) 6146–6153, doi:http://dx.doi.org/10.1158/1078-0432.CCR-08-0509.
[102] H. Huynh, V.C. Ngo, H.N. Koong, D. Poon, S.P. Choo, H.C. Toh, et al., AZD6244 enhances the anti-tumor activity of sorafenib in ectopic and orthotopic models of human hepatocellular carcinoma (HCC), J. Hepatol. 52 (2010) 79–87, doi:http://dx.doi.org/10.1016/j.jhep.2009.10.008.
[103] A. de la Zerda, S. Bodapati, R. Teed, S.Y. May, S.M. Tabakman, Z. Liu, et al., Family of enhanced photoacoustic imaging agents for high-sensitivity and multiplexing studies in living mice, ACS Nano 6 (2012) 4694–4701, doi:http://dx.doi.org/10.1021/nn204352r.

**Quan Zhou** received her B.S. in Applied Biology (Chemistry minor) from Hong Kong Baptist University, Hong Kong. Afterwards, she received her M.S. degree in Biomedical Engineering from University of Michigan, Ann Arbor. She is currently pursuing her Ph.D. in Molecular Imaging Lab at the University of Michigan, Ann Arbor. Her research interests include design and development of novel molecular imaging probes and animal models for targeted hepatocellular carcinoma detection. Quan was awarded the Most Outstanding Active Member by the national engineering honor society, Tau Beta Pi (Michigan Gamma Chapter), in Winter 2013, Fall 2013 and Winter 2014 terms.

**Zhao Li** is an attending surgeon of Peking University People's Hospital hepatobiliary department. His specialty is liver transplantation, liver cancer and portal hypertension. He has finished more than 100 cases of donor liver procurements and is very experienced in treating end-stage liver diseases. In 2010 he engaged in advanced studies of liver transplantation in Cleveland Clinic. Meanwhile, he participated in many basic research of liver cancer and liver transplantation and published several papers in the field.

**Juan Zhou**: My role in this project is to select a panel of peptides that can bind preferentially to cell surface targets that over expressed in liver cancers. I had participated in Human Liver Proteome Project for 3 years when I was pursuing my doctoral degree and have some knowledge about liver cancer biology. Now, I'm involved in developing peptide probes based on purified protein strategy. I have successfully developed protein expression and purification systems, get the purified extracellular domain of EGFR. I am preparing the phage display library screening now. I know something about the structure so that I can try to analysis and choose the target peptide through many candidates and know something about the peptide staining too. In summary, I have obtained substantial training in tumor biology, molecular biology and cell biology, which is highly relevant to this project. My expertise and experience have prepared me to carry out part of this project.

**Bishnu P. Joshi** is a Research Investigator in the laboratory of Dr. TD Wang at the University of Michigan. He earned his PhD in Bioorganic Chemistry from Inha University in Korea, and is an expert in the design, synthesis and validation of novel peptide imaging agents. He supports the development of analytical methods, GLP processes, and stability monitoring for peptides in the clinical study.

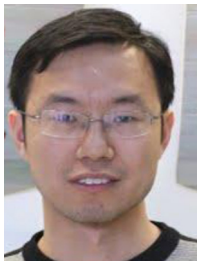

**Gaoming Li's** research field is optical lens designs, optical fiber sensor and laser speckle reduction, and optical lens designs

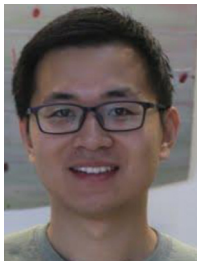

**Xiyu Duan** is currently a Ph.D. student in the Department of Biomedical Engineering at the University of Michigan. He received his B.S and M.S.E. degrees in electrical engineering from Hong Kong University of Science and Technology, Hong Kong and University of Michigan, Ann Arbor, respectively. His research has focused on developing the multi-spectral fiber endoscope to perform targeted surveillance of gastric cancer. He is the recipient of Rackham International Student Fellowship and a co-inventor on two patents.

**Rork Kuick**: Additional areas of Focus: Large RT-PCR studies, and RNA-seq. DNA copy number assays. Mass spectrometry based proteomics and antibody arrays. Assay development. I started research work in the laboratory of Charles Sing, deriving the mathematics for "measured genotype" models and writing specialized software (Algol, Pascal, Fortran) to fit the models to data on lipid levels. Collaborations with (followed by working for) Sam Hanash and James Neel then began an era working on algorithms and user interfaces for measuring, matching, and normalizing spots on proteins separated by 2D gel electrophoresis, as well as performing downstream statistical analysis (MIDAS, SAS, BMDP, and more recently R and Matlab). This spot matching algorithm is still perhaps the fastest and best in the world for many types of problems. I've spent many years as an administrator and programmer of UNIX operating systems (several scripting languages, Perl) and relational database systems (Ingres,Oracle, using PL/SQL emitting mostly HTML/JavaScript, with wrapped C-code or Java for some critical algorithmic pieces) and web sites. Around 1994 we began using large 2D gels to separate genomic DNA ("RLGS"), detecting deletions, amplifications, and methylation changes in cancer or aging, as well as monitoring for germline mutations. I ported and improved my large public image analysis suite (in C, around 40,000 lines) from Sunview to the X-windowing system at this time, thus making it network extensible. In 2000 I began a robots-and-microarrays era, starting with cherry-picking clones and printing DNA microarrays, and then using Affymetrix chips. I'm the author of a publicly available algorithm for extraction of mRNA abundances from Affymetrix arrays, which I used as the first step in analyzing many large studies, as well as approximately 200 smaller studies of a great variety of experimental designs, many with 2 or 3 factors. I believe I am the first person to perform "enrichment testing" on microarray experiments, and was part of a team that made the first publicly available software to perform such testing of GO terms and KEGG pathways. I have measured and analyzed data from large protein microarray experiments and hundreds of blotted 2D patterns searching for autoantibodies in human sera that are useful in diagnosing various cancers, and for which I have invented novel rank-based statistical methods. I have frequently written statistical software in C or C++ that is impractical to perform in higher-level languages. I am experienced in the analysis of large plate-read ELISA studies. I am experienced with multi-channel 2 and 3 dimensional separations of proteins for which I obtain the measurements, perform the pattern matching (with my software), normalization procedures, and statistical analysis. For this and in autoantibody work I also program robots to pick the proteins from gels, and perform the identification searches using the resulting mass spectrometry runs from a wide variety of instruments. I am experienced in the design, scanning, measurement, and analysis of multi-channel antibody microarrays. For most projects I understand the scientific questions, and am able to determine or assist in the experimental designs, performing literature research, and writing papers and grants. I am familiar with a wide variety of bioinformatic tools and techniques regarding sequence similarity, homolog or paralog mapping, functional gene or protein annotation, linkage analysis, transcription binding site mapping, and other tasks common in the analysis of data-sets involving hundreds or thousands of genes or proteins.

**Scott R. Owens** received a B.S. in biology from Calvin College in Grand Rapids, Michigan in 1994 and an M.D. from Wayne State University in Detroit, Michigan in 1999. His residency and fellowship training in Anatomic and Clinical Pathology at the University of Michigan included fellowships in Surgical Pathology, Hematopathology and Gastrointestinal Pathology, which he completed in 2006. He joined the faculty of the Department of Pathology at the University of Pittsburgh Medical Center as an Assistant Professor in July 2006 and spent more than four years at that institution, where he participated actively in medical student and resident teaching and developed research interests in hematolymphoid neoplasms of the gastrointestinal tract and liver, inflammatory bowel disease, pancreaticobiliary neoplasia, and patient safety and quality assurance in surgical pathology. In October 2010, Dr. Owens joined the faculty of the University of Michigan Department of Pathology as an Assistant Professor, and in September 2013, he was promoted to Associate Professor. Currently, he serves as the Director of the Division of Quality and Health Improvement and the Medical Director of Professional Practice Evaluation. He is a graduate of the Patient Safety and Quality Leadership Scholars program offered by the Department of Learning Health Sciences at the University of Michigan, and is the author of more than 60 peer-reviewed publications, books, book chapters and abstracts. Dr. Owens has been invited on numerous occasions to deliver extramural, national and international presentations. He is board certified in Anatomic and Clinical Pathology, and in Hematopathology.

**Thomas D. Wang**, MD, PhD is the H. Marvin Pollard Collegiate Professor of Endoscopy Research and Professor of Internal Medicine, Biomedical Engineering, and Mechanical Engineering at the University of Michigan. He earned his Bachelor's degree in mathematics and physics from Harvey Mudd College, and his Master's in Electrical Engineering from MIT. He completed his PhD in Medical Engineering/Medical Physics (MEMP) at the G.R. Harrison Spectroscopy Lab at MIT under Professor Michael S. Feld. He earned his medical degree (MD) from Harvard Medical School in Health Sciences and Technology (HST). He completed his residency in internal medicine at Boston University and fellowship in gastroenterology at Stanford University. He is a physician scientist who has developed a number of novel methodologies for in vivo imaging in the digestive tract for early cancer detection and staging. He has pioneered the use of fluorescence-labeled peptides to detect overexpressed cell surface targets in vivo to identify pre-malignant mucosa. Furthermore, he has developed the first video endoscope that is sensitive to fluorescence for rapidly identifying pre-malignant lesions over large mucosal surface areas. This approach has been patented, commercialized, and developed for clinical use, and is widely cited as a major impetus for the accelerated convergence of fluorescence spectroscopy and endoscopy. He has mentored a total of 3 junior faculty (research investigators), 25 post-docs (research fellows), 4 M.D. (clinical) fellows, 10 graduate students, 2 medical residents, 2 medical students, and 6 undergraduates. In addition, he has filed 13 patents with the US Patent & Trademark Office (USPTO) on novel optical imaging technologies.